Aerodynamic Analysis and Design Optimization of a Novel Flapping Wing Micro Air Vehicle in Hovering Flight

Y. Zhang[1], Z. Wang[2†] and H. Zheng[1]

[1] *Mechanical and Electrical Engineering Department, University of Electronic Science and Technology of China, Chengdu, Sichuan, 611731, PR China*
[2] *Mechanical and Electrical Engineering Department, University of Electronic Science and Technology of China, Huzhou, Zhejiang, 313001, PR China*

†*Corresponding Author Email: wzhonglai@uestc.edu.cn*

ABSTRACT

Inspired by the challenging and nimble flight dynamics of flying insects and birds, this research investigates bionic propulsion technology to develop an improved flapping wing micro air vehicle (FWMAV) design. Following the bionic formula, a prototype is preliminarily designed to achieve multi-attitude flight. Then, kinematic modeling is employed for further data analysis. A meshless particle hydrodynamics method is adopted to explore an optimized flapping driving mechanism and understand the influence of the flapping frequency, flapping amplitude, and quick-return characteristics of one side of the symmetrical mechanism on aerodynamic performance. Based on the aerodynamic model, force measurement experiments are developed to verify simulation availability and investigate the importance of wing flexibility. The numerical analysis results demonstrate that the average lift is approximately proportional to the flapping frequency, flapping-wing amplitude, and quick-return characteristics. Further optimization is conducted to find the best design parameters setting because of the complicated coupling relationship between the flapping wing amplitude and quick-return characteristics. Moreover, the optimized wing property supports high aerodynamic performance via experimental analysis in hovering flight.

NOMENCLATURE

AR	Aspect Ratio	S	wing area
a	crank length	s	wingspan
b	connecting rod length	α, β	vein angle
C_R	wing root length	θ	angle between the crank and the connection line
C_T	wing tip length		
c	rocker length	φ	flapping amplitude
d	frame length	γ	transmission angle when the crank and rack coincide collinearly
F	wing load		
f	flapping frequency	ω	rocker angular velocity
k	level of quick-return characteristic	ε	angular acceleration of the connecting rod and joystick
L_{LE}	leading edge length		
L_{TE}	trailing edge length		

1. INTRODUCTION

Various flying and swimming animals in nature, including birds, insects, fish, and marine mammals, have evolved over several hundred million years, experiencing a long process of environmental adaptation and natural selection (Shyy *et al.* 2013). Bionics is an old and young subject. The structure and functional mechanism of creatures promote new equipment, tools, and technologies. If explored as a

living machine, the animal is a kinematic chain capable of autonomous flight or swimming. It is a complex system that includes neural control, muscle mechanics, biological materials, animal morphology and kinematics, animal external fluid mechanics, and energy conversion and efficiency. Studying the design principles and related theories of complex kinematic chain systems provides a theoretical basis for bionics. This is a major interdisciplinary issue with major engineering needs. Therefore, studying air or underwater vehicles based on biological characteristics is necessary and has bright prospects (Apker and Corke 2015; Li *et al.* 2022).

This research mainly focuses on flying biomechanics, and its significance is multifaceted. Biomimetics has been rapidly emerging and needs to be supported by theories in this discipline. In recent decades, the development of bionic machines has progressed by leaps and bounds. On the other hand, engineers can improve man-made machines with biomechanical technology. Many significant advances have been made in bionic birds, insects, and fishes. Some excellent experimental prototypes have been successfully produced, and some have been transformed into products for national defense or business use (Perçin *et al.* 2016; Shahzad *et al.* 2019; Martínez Gallar *et al.* 2020).

The study of biomimetic flapping wing micro air vehicles (FWMAVs) is a core field of flying biomechanics in engineering applications. Bionic flapping wings can be understood as the mechanical reconstruction of certain insects or birds through bionics to imitate their flight behavior. It is a new interdisciplinary subject comprising many disciplines, such as mechanics, biology, materials science, control theory, energy technology, and advanced manufacturing, with fluid mechanics as the forerunner. With the development of micro air vehicles (MAVs) and bionic machines, this subject has received much attention internationally. Some in-depth discussions on the subject development strategy have also been completed to promote research in this area (Kumar and Shah 2017; Syam Narayanan and Ahmed 2021).

FWMAV has replaced fixed and rotor wing MAVs as a research hotspot. FWMAVs have many advantages over fixed or rotor wing MAVs, including micro miniaturization, mobility, adaptability, maneuverability, concealment, and energy efficiency (Cho *et al.* 2016). With the development of the flapping flight mechanism, microelectromechanical system technology (MEMS), aerodynamics, and materials technology, FWAMV is developing rapidly.

Landmark designs on FWMAVs (e.g., Nano Hummingbird, FlowerFly, Dragonfly, DelFly series, and Festo MAV series) have been implemented (Ellington 1984; Wang *et al.* 2004; Seshadri *et al.* 2013; Nguyen *et al.* 2017; Phan *et al.* 2017; Cros *et al.* 2018; Dong *et al.* 2022). The flapping action of Nano Hummingbird is realized by the traditional motor combined with the rope drive, which is simpler and more efficient than the rod drive

(Keennon *et al.* 2012). Zhang *et al.* (2015) developed a motor-driven FWMAV, where two micro-motors drive the connected first-level deceleration system to realize the flapping motion on both sides. DelFly II has a more extensive flight range, despite its small wing length (28 cm long) and lightweight (16 g). It can even achieve hovering and inverted flight and can last for approximately 15 min (Armanini *et al.* 2016; Kajak *et al.* 2019).

A comprehensive review of the aerodynamics of flapping and fixed wings has been accomplished (Sane 2003; Heathcote and Gursul 2007; Shyy *et al.* 2016; Arastehfar *et al.* 2019). Moreover, researchers have reviewed the advantages, disadvantages, and development directions of FWMAVs (Floreano and Wood 2015; Mayo *et al.* 2015; Kumar and Shah 2017). These investigations have associated aerodynamic phenomena with unsteady motions (Deng *et al.* 2017; Qadri *et al.* 2019).

To accomplish 3D aerodynamic analyses of the flapping wing, Combes and Daniel (2003) investigated the wing's bending condition and degree of bending and found that the inertial force controls the wing's deformation. Tay *et al.* (2015) studied the DelFly Micro and found that increasing the aircraft's pitch angle creates more lift. Additionally, they found that simultaneous changes to the span and chord can generate the optimum thrust. Liu *et al.* (2019) described a novel FWMAV and conducted aerodynamic analyses to identify the effects of angle of attack, wind speed, and flapping frequency on the lift in a flapping-wing flight. A NACA0012 airfoil consisting of sequential translations and rotations was considered by Bharadwaj and Ghosh (2020) to determine the effects of rotational characteristics on aerodynamics.

However, studies on the effect of quick-return characteristics (representing the time ratio between up and down strokes) of flapping driving mechanisms are relatively limited. In addition, the study of wing flexibility overlooks vein effects.

The novelty of the present paper is threefold: (1) a novel FWMAV design including a flapping driving mechanism, dihedral angle control mechanism, and pentagon-like wings is proposed; (2) a validated and efficient aerodynamic model and an experimental platform are developed; (3) a parametric analysis for the effects of quick-return characteristics and vein characteristics is conducted.

The remaining paper is organized as follows. Section 2 describes the proposed FWMAV, aerodynamic, and experimental models. Section 3 presents the results and discussions of unsteady force analysis and optimization. Section 4 concludes the paper.

2. MODEL AND METHOD

2.1 Mechanical Model

2.1.1 Mechanical Design

The methods used in this study and the procedures for data analysis are listed below:

Table 1 Initial physical parameters of FWMAV.

	Wingspan	Wing area	Aspect ratio	Wing load	Flapping frequency
Dimensions	m	m^2	-	N/m^2	Hz
Equation	$2.24\ m_b^{0.53}$	$0.69\ m_b^{1.04}$	$7.28\ m_b^{0.02}$	$17.3\ m_b^{-0.04}$	$1.32\ m_b^{-0.60}$
Value	0.3492	0.0186	6.7869	19.2191	10.8

Step 1: Mechanical design of FWMAV comprising a flapping driving mechanism, dihedral angle control mechanism, and pentagon-like wings

Step 2：Aerodynamic model allows meshless simulation, experiment validation, and experimental explorations for clapping-typed FWMAV to determine the effects of flapping frequency wing amplitude, quick-return characteristics, and wing layout on aerodynamic characteristics.

Step 3: The optimization model identifies the optimal flapping parameters for a larger average lift based on aerodynamic analysis.

The designed FWMAV has a mass of approximately 30 g. Inspired by FlowerFly and DelFly Nimble, a clapping-wing-type FWAMV was designed for high aerodynamic performance and stability (Karásek *et al.* 2018). We replaced the circular servos in DelFly Nimble with linear servos to increase the stability of the aircraft and improve the flapping wing driving mechanism. The functional relationship among biological structure, motion parameters, and mass proposed by Shyy *et al.* (1999) was used. These bionic equations describe the relationship between flight parameters and body mass m_b, which is useful for specifying initial parameters. The calculated physical parameters of FWMAV are listed in Table 1. The motion posture of a dragonfly consists of three components: pitch, yaw, and torsion motion. Therefore, to better simulate the motion of a dragonfly, a multi-attitude flight control mechanism is preliminarily designed (Fig. 1a), including a pitch control mechanism (Fig. 1b) and a yaw

control combing with the tail wing design. Conventional flapping driving mechanisms can be motor, piezoelectric, memory alloy, or artificial muscle-type actuation. Considering the dimensional law and Reynolds number of the flapping model, a motor drive with a rigid connecting rod is used, and a gear reduction system is adopted as the transmission mode. Recently, double-crank and double-rocker mechanisms have become the priority for conducting flapping driving mechanisms.

Motion analysis of the predesigned FWMAV is subsequently carried out. Since the flapping wing mechanism is symmetrical, it is sufficient to investigate the left half only. This choice can also reduce wing-wing effects to make the results more accurate. Figure 2 shows a schematic of the upper and lower limit position mechanism of the left half-flapping driving mechanism. O_1A, AB, and BO_2 are the crank, connecting rod, and rocker, respectively. x and y are the vertical and horizontal distances, respectively, between the crank and rocker rotation centers. θ is the angle at which the crank rotates relative to the connection line, and φ is the angle between the rocker and horizontal plane, namely, the flapping wing amplitude.

At the upper limit position, with the wing flapping to the highest point, the crank and the connecting rod stretch collinearly, and the geometric relationship is given by Eqs. (1) and (2).

$$\varphi_a = \arccos\left[\frac{O_1O_2^2 + BO_2^2 - (AB + AO_1)^2}{2O_1O_2 \times BO_2}\right]$$
$$- \arctan\frac{y}{x} \tag{1}$$

$$\theta_a = \arccos\left[\frac{O_1O_2^2 + (AB + AO_1)^2 - BO_2^2}{2O_1O_2 \times (AB + AO_1)}\right] \tag{2}$$

At the lower limit position, with the crank and connecting rod collinear at the lowest point of wing
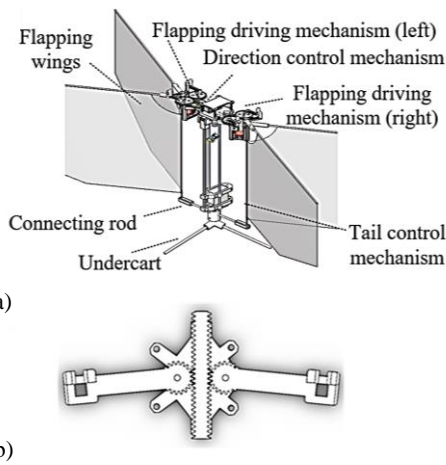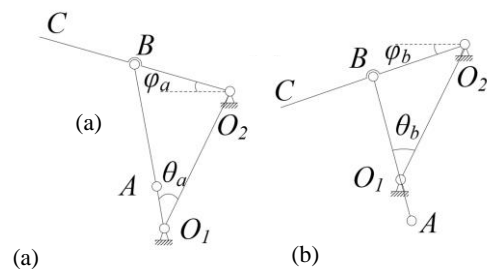

(a)

(b)

Fig. 1. (a) Schematic of the multi-attitude flight control prototype, and (b) schematic of dihedral angle control mechanism based on the linear servo.

(a)

(b)

Fig. 2. Schematic of the flapping driving mechanism.

flapping, the geometric relationship is described by Eqs. (3) and (4).

$$\varphi_b = \arccos\left[\frac{O_1O_2^2 + BO_2^2 - (AB - AO_1)^2}{2O_1O_2 \times BO_2}\right] \\ - \arctan\frac{y}{x} \tag{3}$$

$$\theta_b = \arccos\left[\frac{O_1O_2^2 + (AB - AO_1)^2 - BO_2^2}{2O_1O_2 \times (AB - AO_1)}\right] \tag{4}$$

The crank angle of the rocker from the upper to the lower limit position can be calculated using Eq. (5).

$$\theta_{down} = \pi + \theta_a - \theta_b \\ = \pi + \arccos\left[\frac{O_1O_2^2 + (AB + AO_1)^2 - BO_2^2}{2O_1O_2 \times (AB + AO_1)}\right] \\ - \arccos\left[\frac{O_1O_2^2 + (AB - AO_1)^2 - BO_2^2}{2O_1O_2 \times (AB - AO_1)}\right] \tag{5}$$

Now, a set of nonlinear equations is established according to φ_a, φ_b, and θ_{down}. The length of each rod can be obtained: $AO_1 = 4.8$ mm, $AB = 12.6$ mm, and $BO_2 = 12.4$ mm using the MATLAB solving function; the angle is calculated using Eqs. (1) – (5). To further check whether it meets the basic mechanical design requirements, the transmission angle in Eqs. (6) and (7) are calculated.

$$\gamma = \arccos(\frac{AB^2 + BO_2^2 - (O_1O_2 - AO_1)^2}{2AB \cdot BO_2}) \tag{6}$$

$$\gamma' = \arccos(\frac{AB^2 + BO_2^2 - (O_1O_2 + AO_1)^2}{2AB \cdot BO_2}) \tag{7}$$

where γ is the transmission angle when the crank and the rack coincide collinearly and γ' is the transmission angle when the crank and the frame are elongated and collinear.

Substituting in $\gamma_{min} = \min\{\gamma, 180 - \gamma'\}$, the value of 54.9 deg, satisfies the requirement of an allowable transmission angle. All the rod length parameters were found to meet the design requirements. Coupled with a two-stage reduction mechanism with a gear reduction ratio of 19.75, a flapping driving mechanism is preliminarily finished (Fig. 3a).

Using ADAMS to perform motion kinematics simulation, the two rocker movement curves can be acquired. The angular velocity curve is given in Fig. 3(b). The rocker angular velocity curve is approximately coincidental, and the movement is relatively smooth. After completing the design of the flapping driving mechanism and the dihedral angle control mechanism, the flapping wing is designed, which also directly affects the aerodynamic performance. The wings of insect-like FWMAVs are mainly divided into triangles, sectors, and trapezoids. The trapezoid type is adopted, and some improvements are made, as shown in Fig. 4,
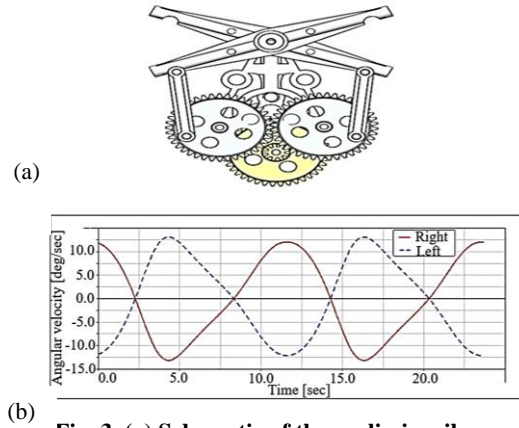
(a)

(b)

Fig. 3. (a) Schematic of the preliminarily designed flapping driving mechanism, and (b) time histories of the angular velocity of the rocker.

including leading edge length L_{LE}, trailing edge length L_{TE}, wing root length C_R, and wing tip length C_T. According to the bionics formula mentioned, the estimated values of the wingspan and wing area are 0.3492 m² and 0.0186 m², respectively. Since the lateral dimensions of the flapping driving mechanism are 0.08 m, the effective wingspan length is defined to be 0.28 m. Thus, L_{LE} = 0.14 m, $L_{TE} = 0.065$ m. The wing chord length is 0.088 m using the trapezoidal area formula, and the wing tip size is 0.058 m. Since the chord length is calculated by the trapezoidal formula, the actual wing area is different from the estimated value obtained by the bionic formula. The actual wing area is 0.0224 m², slightly larger than the estimated value. Considering that a large area brings more lift, we assume that the demands are met.

2.1.2 Motion Kinematics

The FWMAV comprises two symmetrical flapping driving mechanisms, which affect the lift, and a yaw control mechanism. Considering the complexity of wing-wing effects and the interaction of mechanical vibration, the FWMAV with only one flapping wing-
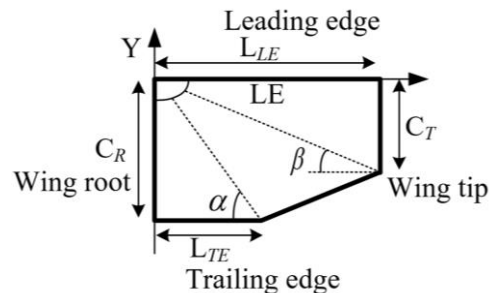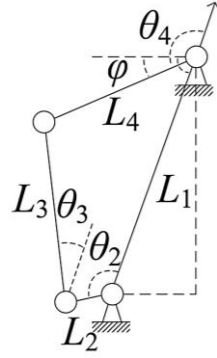
Fig. 4. Schematic of the pentagon-like wing.

Fig. 5. Schematic of the left half of the flapping driving mechanism.

mechanism is the test model instead of the clapping wing FWAMV (Fig. 3a). The flapping driving mechanism in this paper is a double-crank and double-rocker mechanism. Because of its symmetry, the left half is taken for further data analysis. Figure 5 shows the kinematics of the mechanism. In the schematic diagram, L_1 is the frame, L_2 is the crank, L_3 is the connecting rod, and L_4 is the rocker. A Cartesian coordinate system is established along L_1 and the direction perpendicular to it; θ_2 is the crank angle, θ_4 is the rocker angle, and φ is the flapping angle.

The closed-loop vector position equation of the mechanism is established using Eq. (8).

$$\vec{L_2} + \vec{L_3} = \vec{L_1} + \vec{L_4} \tag{8}$$

The component form of the angular displacement can be obtained using Eq. (9).

$$L_2\cos\theta_2 + L_3\cos\theta_3 = L_1\cos\theta_1 + L_4\cos\theta_4$$
$$L_2\sin\theta_2 + L_3\sin\theta_3 = L_1\sin\theta_1 + L_4\sin\theta_4 \tag{9}$$

Because $\theta_1 = 0$ and θ_2 is already known, we can obtain Eq. (10).

$$\begin{cases} f_1(\theta_3, \theta_4) = L_2\cos\theta_2 + L_3\cos\theta_3 \\ \quad -L_1 - L_4\cos\theta_4 = 0 \\ f_1(\theta_3, \theta_4) = L_2\sin\theta_2 + L_3\sin\theta_3 \\ \quad -L_4\sin\theta_4 = 0 \end{cases} \tag{10}$$

By substituting the crank angle θ_2, the angle φ between the connecting rod and rocker can be obtained using Eq. (11). φ is also called flapping angle or amplitude.

$$\varphi = \theta_4 - (180° - \gamma) = \theta_4 + \gamma - 180° \tag{11}$$

where $\gamma = \arctan(y/x)$ is the angle between the rack and horizontal direction.

Using the component form of the closed-loop vector angular displacement equations to find the first derivative with respect to time is given in Eq. (12).

$$-L_3\omega_3\sin\theta_3 + L_4\omega_4\sin\theta_4 = L_2\omega_2\sin\theta_2$$
$$L_3\omega_3\cos\theta_3 - L_4\omega_4\cos\theta_4 = -L_2\omega_2\cos\theta_2 \tag{12}$$

where ω represents the corresponding angular velocity.

The equivalent matrix form is given in Eq. (13).

$$\begin{pmatrix} -L_3\sin\theta_3 & L_4\sin\theta_4 \\ L_3\cos\theta_3 & -L_4\cos\theta_4 \end{pmatrix}\begin{pmatrix} \omega_3 \\ \omega_4 \end{pmatrix} = \begin{pmatrix} \omega_2 L_2\sin\theta_2 \\ -\omega_2 L_2\cos\theta_2 \end{pmatrix} \tag{13}$$

Then, the angular velocity expressions of the connecting rod and rocker are presented using Eq. (14).

$$\omega_3 = -\omega_2 L_2\sin(\theta_2 - \theta_4) / [L_3\sin(\theta_3 - \theta_4)]$$
$$\omega_4 = \omega_2 L_2\sin(\theta_2 - \theta_3) / [L_4\sin(\theta_4 - \theta_3)] \tag{14}$$

From the component form of the closed-loop vector angular displacement equations, the second derivative of time is obtained and converted to the matrix form in Eq. (15).

$$\begin{pmatrix} -L_3\sin\theta_3 & L_4\sin\theta_4 \\ L_3\cos\theta_3 & -L_4\cos\theta_4 \end{pmatrix}\begin{pmatrix} \varepsilon_3 \\ \varepsilon_4 \end{pmatrix} =$$
$$\begin{pmatrix} L_2\omega_2^2\cos\theta_2 + L_3\omega_3^2\cos\theta_3 - L_4\omega_4^2\cos\theta_4 \\ L_2\omega_2^2\sin\theta_2 + L_3\omega_3^2\sin\theta_3 - L_4\omega_4^2\sin\theta_4 \end{pmatrix} \tag{15}$$

The angular acceleration of the connecting rod and the joystick ε can be expressed using Eq. (16).

$$\varepsilon_3 =$$
$$\frac{-\omega_2^2 L_2\cos(\theta_2 - \theta_4) - \omega_3^2 L_3\cos(\theta_3 - \theta_4) + \omega_4^2 L_4}{L_3\sin(\theta_3 - \theta_4)}$$
$$\varepsilon_4 =$$
$$\frac{\omega_2^2 L_2\cos(\theta_2 - \theta_3) - \omega_4^2 L_4\cos(\theta_4 - \theta_3) + \omega_3^2 L_3}{L_4\sin(\theta_4 - \theta_3)} \tag{16}$$

Motion kinematics is the basis for further simulation and optimization.

2.2 Aerodynamic Model

Based on the preliminary design, analysis, and optimization of the two key pneumatic FWMAV components, namely, the flapping wing driving mechanism and the wing design parameters, are conducted. Considering that flapping flight is a high-frequency process, the meshless method has unique advantages in solving N-S equations with large displacements. XFLOW software is based on particle hydrodynamics, which is an efficient meshless method. Thus, it is no longer necessary to mesh the fluid field. Moreover, the particle's physical properties are estimated by interpolating the values of its nearest neighbors using continuous and differentiable interpolation functions. These functions are used to interpolate fluid velocity, pressure, density, temperature, and other field parameters requiring interpolation. This characteristic gives XFLOW the ability to handle
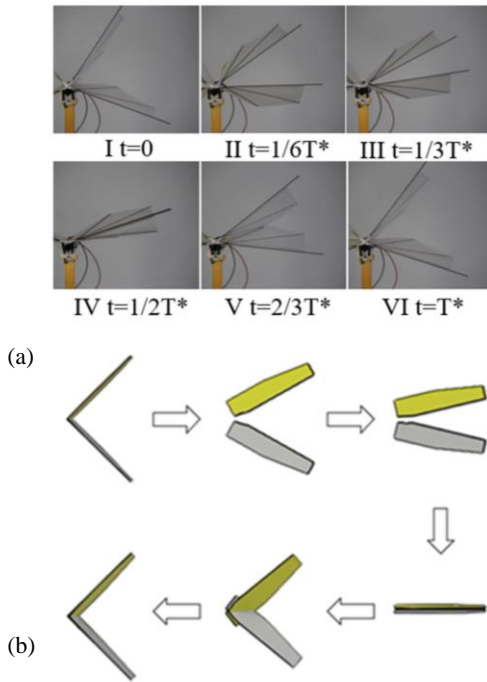
(a)

(b)

Fig. 6. Motion decomposition during a cycle (a) experiment and (b) aerodynamic model

fluid-structure interaction problems. Considering that XFLOW can handle moving objects and build fluid-structure interaction models, it becomes the aerodynamic solver for solving unsteady flows.

When modeling the FWMAV in XFLOW, the model should reflect the actual motion. Since it is difficult to restore flexible deformation under all parameter combinations, images of a complete cycle at 12 Hz (Fig. 6a) are regarded as the reference considering that the deformation is clear and reliable. Cubic and linear interpolation functions combined with Eqs. (10) and (11) are used to represent clap and reverse motions to simulate this real flapping motion. The superposition of Eqs. (10) and (11) can restore the real motion to a large extent. Figure 6(b) shows the simulated images corresponding to the experimental images. In addition, some other key simulation setups are given below. First, a hovering state is assumed. Second, the solver is set to 3D unidirectional constant temperature outflow, and the turbulence model is set as the Spalart-Allmaras model. The simulated wind tunnel size is $0.5 \text{ m} \times 0.75 \text{ m} \times 0.5 \text{ m}$, where the fluid medium is air, the temperature is 288.15 K, and the density is 1.225 kg/m^3. The inlet of the virtual wind tunnel is et as the velocity boundary, which is taken as 0 m/s. In addition, the outlet is set as the pressure outlet. The dynamic viscosity coefficient is equal to $1.789 \times 10^{-5} \text{ Pa} \cdot \text{s}$. Figure 7 describes the chordwise flow field at t=1/6T*, 1/2T*, and T* to show the movement of the vortex. The focus of this paper is the influence of the flapping frequency, flapping amplitude, and level of quick return on aerodynamic

characteristics, especially under instantaneous and average lift conditions.

2.3 Experimental Setup

In addition to the simulation, an experiment was conducted to estimate the evolution of unsteady forces for the given kinematics. The experimental setup is shown in Fig. 8 (a). The experiment verifies the aerodynamic model and further studies the influence of wing flexibility on the aerodynamic characteristics of FWMAVs. The layout and the difference in the stiffness of the wing veins characterize flexibility. Forces are measured using a Nano17 F/T transducer, one of the smallest 6-axis sensors in the world. Force signals are acquired at a 2 kHz data acquisition frequency via a filter. Ensemble averaging of forces is performed over ten repetitions of the experiments. The averaged force data is then filtered using a Chebyshev Type II low pass filter with a variational cut-off frequency to remove electrical noise and mechanical vibrations.

There are various wing vein layout schemes for FWMAVs. The chosen scheme includes two wing veins to connect the leading edge and inflection point of the wing edge. Regarding the inflection point as the endpoint, the different combinations of angle (
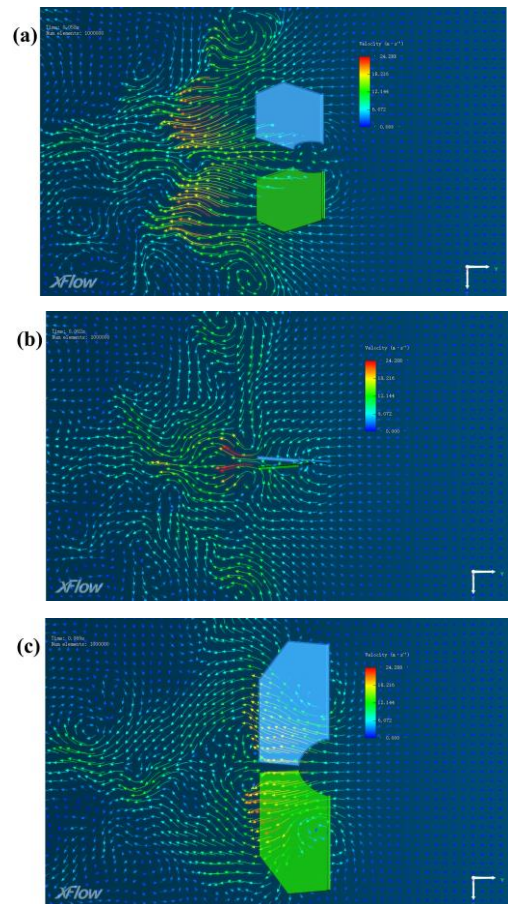

(a)

(b)

(c)

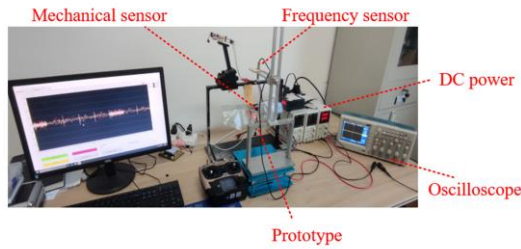**Fig. 7. (a) Chordwise flow field at (a) t=1/6T*, (b) (c)t=1/2T*, and (c) t=T*.**

Fig. 8. Experimental platform of the force and energy consumption measurement.

α, β)are defined as different wing vein layouts. A special naming rule is $\mathrm{Wing} + \alpha + \beta$, as shown in Fig. 4. It shows a wing vein layout scheme called Wing5424, where $\alpha = 54$ deg，$\beta = 24$ deg.

In addition, a change in the stiffness of the wing veins can influence flexibility. Researchers have shown that the wing vein size is between 0.5 mm and 1 mm for FWMAVs of similar size and weight.

3. RESULTS AND DISCUSSION

3.1 Evolution of Unsteady Forces Under Simulation

The graph of the first three periods of instantaneous lift, with the flapping amplitude fixed at 45 deg and no quick-return characteristic, is shown in Fig. 9.
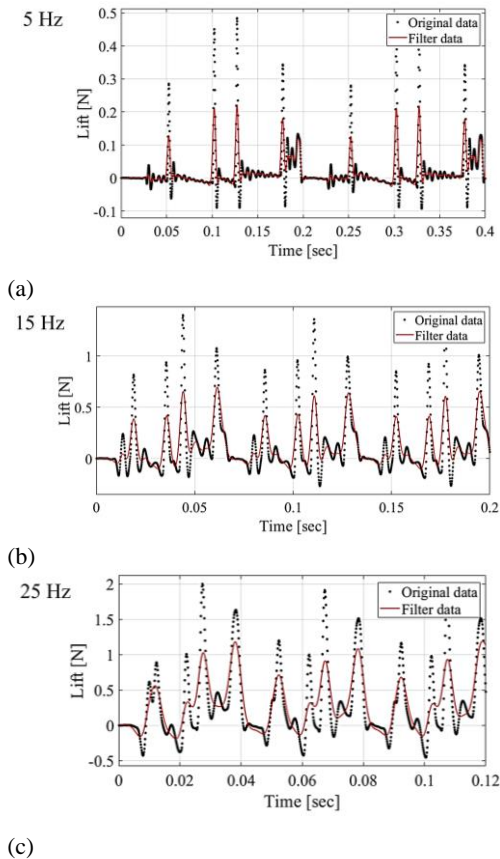

(a)

(b)

(c)

Fig. 9. Time histories of lift at various flapping frequencies.

Figure 10 (a) shows changes in the average lift with flapping frequency. As the flapping wing frequency increases from 5 to 25 Hz, the average and peak lift increase steadily. The number of crests and troughs increases during the same flutter. The absolute value of the crest is 5-7 times larger than that of the previous value.

Next, the influence of the flapping amplitude on the aerodynamic characteristics is analyzed by setting the flapping frequency to 20 Hz with no quick return at first. The proposed simulation performs 7 sets of simulations with a flapping amplitude ranging from 35 to 65 deg. Figures 9(b) and 10(b) show the changes in the instantaneous lift curve and average lift with the flapping amplitude, respectively. Within the range, the fluctuation law of each lift curve with increasing flapping amplitude is unchanged. However, the overall lift generated when the flapping wings are closed increases, and the peak of negative lift during the twisting phase decreases. The average lift amplitude gradually increases with increasing flapping amplitude.

In this research, the level of quick return characteristics of the flapping driving mechanism is defined by Eq. (17).

$$k = \frac{t_{Folding}}{t_{Separating}} \tag{17}$$
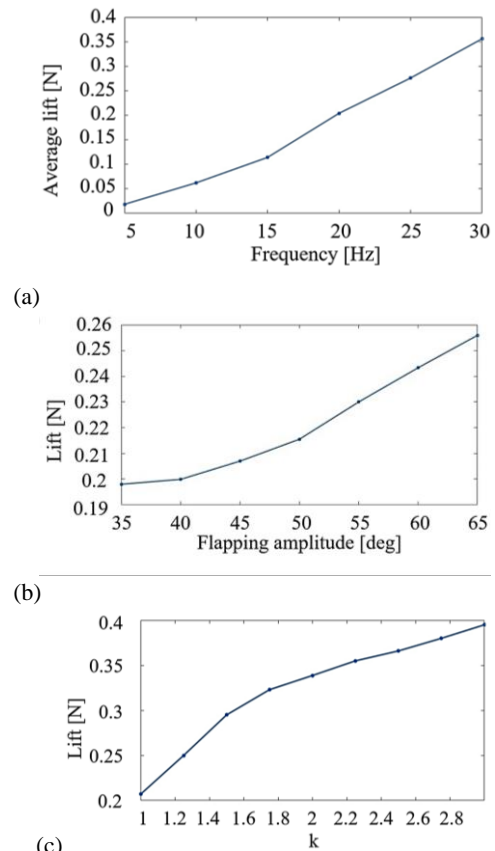

(a)

(b)

(c)

Fig. 10. Average lift with (a) flapping frequencies, (b) flapping wing amplitudes, and (c) levels of quick-return characteristics.

where k is the quick-return characteristic, $k > 1$ represents the quick-return of folding, $k < 1$ represents the quick-return of separating, and $k = 1$ represents no quick-return. The parameter $t_{Folding}$ is the time required for the two flapping wings to move together in a period, and $t_{Separating}$ is the time required for the two flapping wings to move apart in a period.

Some research studies have found that the closing phase generally accounts for 60 % - 80 % of a complete flapping cycle, so k is varied from 1.5 to 3.0. $k = 1$ is chosen as the control group. The average lift change curve in Fig. 10(c) are compared. The instantaneous lift change graph in Fig. 11. As the level of quick return increases, the peak lift generated by the flapping wing rises. The time of the negative lift generation phase becomes correspondingly shorter, while that of the positive lift generation phase becomes correspondingly longer, influencing the lift.
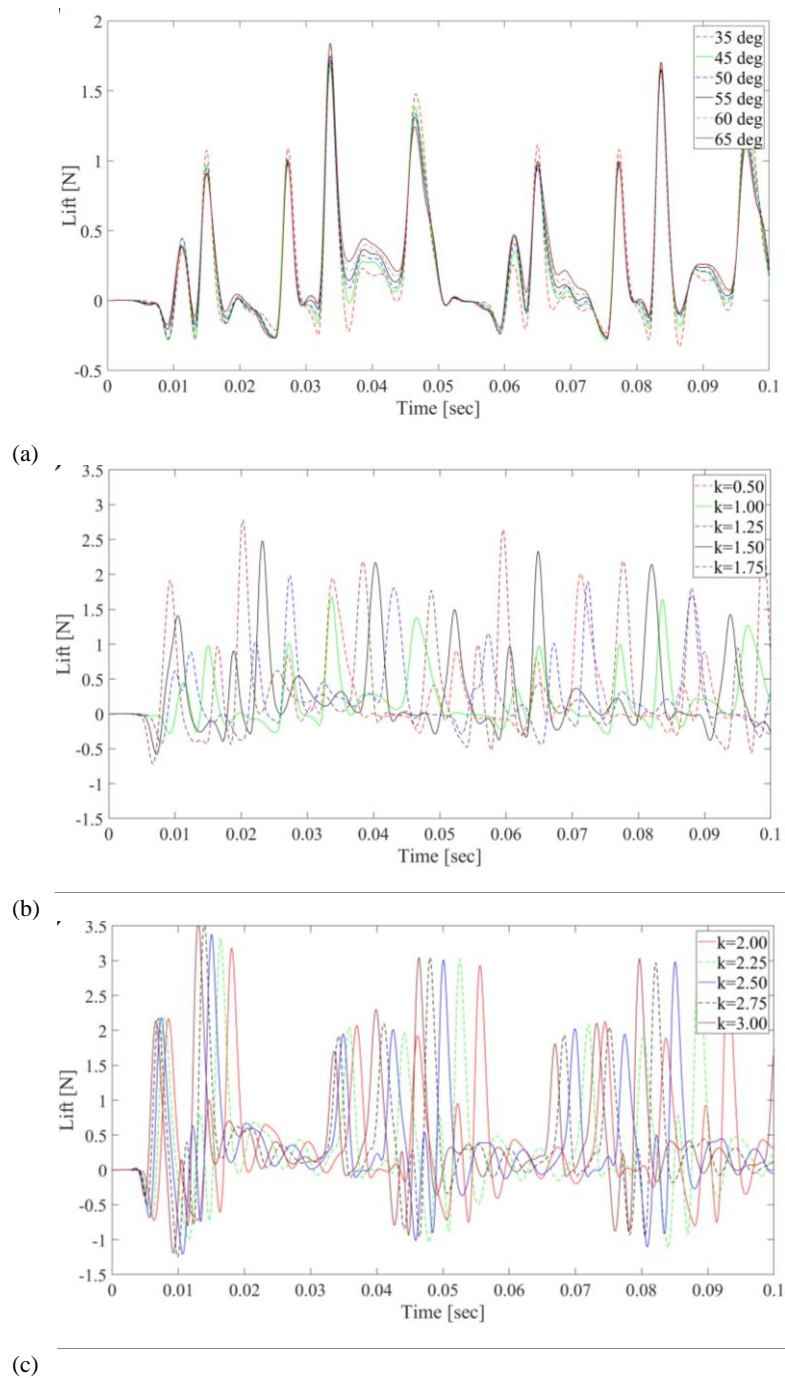

(a)

(b)

(c)

Fig. 11. Time histories of lift at (a) various flapping wing amplitudes, (b) and (c) various levels of quick-return characteristics.
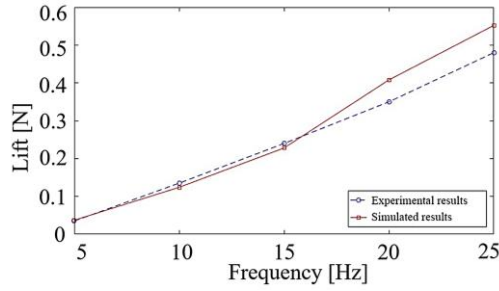
Fig. 12. Comparison of the average lift obtained from experimental and aerodynamic models at various frequencies.

In Fig. 10 (c), as the level of quick-return increases, the average lift increases. However, it is unclear whether higher-level quick-return characteristics improve aerodynamic performance as the driving torque and inertia moment of the flapping driving mechanism are also increased, especially during the rapid return motion stroke. Therefore, adopting large quick-return levels require further investigation.

3.2 Evolution of Unsteady Forces under Experiment

The goal of an experimental platform was to verify the simulation and determine the wing flexibility. As shown in Fig. 11, the experimental results and aerodynamic simulation results have a high degree of conformity. Within our working conditions (from 5 to 25 Hz) in Fig. 12, the difference between the experimental and simulation data will increase with increasing flapping frequency. This is because, in the actual experiment process, the FWMAV will experience some additional vibration at high frequencies, which reduces aerodynamic forces. However, this difference is within the acceptable range. Therefore, the accuracy of the proposed simulation model is high.

Two wing veins are arranged in parallel to understand how the vein layout affects flexibility. The flapping wing frequency range is set from 5 to 14 Hz for aerodynamic experiments with a 30 s experimental time. Figure 13 (a) indicates that Wing3535 owns the highest average lift and Wing00 has the worst aerodynamic characteristic. The main disadvantage of Wing00 is the enhanced spanwise stiffness and almost constant chord stiffness. Hence, when the wing flaps, the chordwise wing is deformed by air resistance, and the generation area of lift is reduced, causing a smaller lift. Moreover, Wing3535 and Wing6565 have relatively good wing vein layouts. Other typical wing layouts (Wing5035, Wing5065, Wing6535, Wing6550, Wing7832, Wing8235, and Wing8638) are also considered, as shown in Fig. 13 (b). The increased divergence of the two wing veins worsens aerodynamic performance. Wing6535 and Wing8235 reach the best aerodynamic values. Further experiments demonstrate that the energy consumption of Wing8235 is lower and is adopted as the final layout.
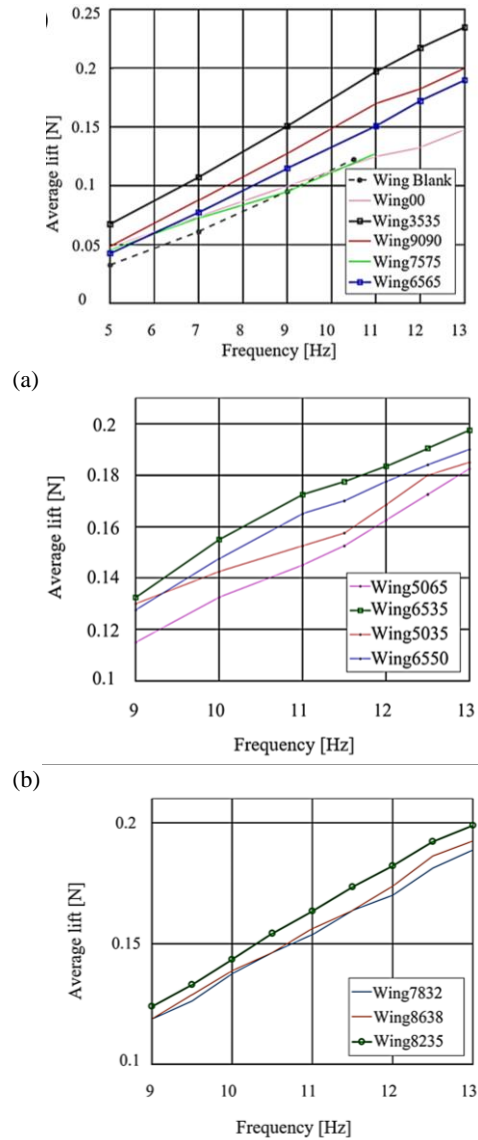

(a)

(b)

(c)

Fig. 13. (a) Measured average lift of different wing layouts at various flapping frequencies ($\alpha = \beta$), and (b) measured average lift of some typical wing layouts.

Another factor influencing aerodynamic performance is wing vein stiffness. When the length of the wing veins is fixed, the stiffness is mainly reflected by the different diameters of the wing veins. Therefore, the experimental scheme is set according to the different diameters of the wing veins on Wing8235. The experimental scheme in Table 2 shows decreasing flexibility. The aerodynamic experimental results are shown in Fig. 14 (a).

As flexibility decreases ([0.5, 0.8], [0.5, 1.0], and [0.8, 0.8]), the average lift first rises and then stabilizes. To further determine the optimized plan, the energy consumption of these three groups is measured again. The lift/energy consumption ratio is shown in Fig. 14 (b). A wing vein diameter of [0.5, 0.8] represents the optimized scheme, which is selected in the designed FWAMV to maximize aerodynamic performance.
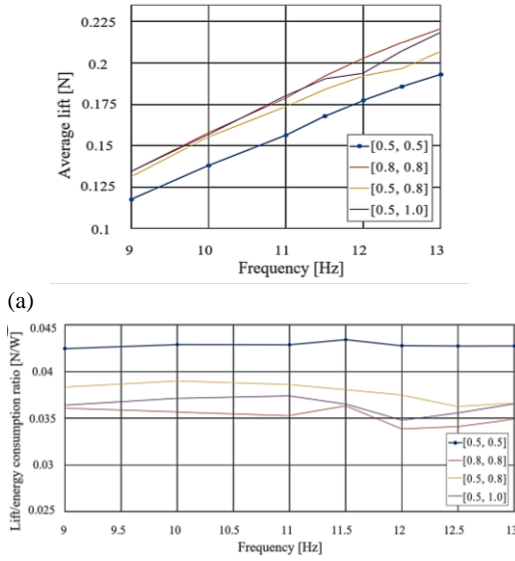
(a)

(b)

Fig. 14. (a) Measured average lift of different wing stiffnesses at various flapping frequencies and (b) measured average lift/energy consumption ratio of different wing stiffnesses at various frequencies.

3.3 Aerodynamic Optimization of the Flapping Driving Mechanism

The flapping driving mechanism can determine the flapping frequency, flapping amplitude, and level of quick-return characteristics. From the simulation analysis, an increase in all three parameters positively influences lift generation. It can be concluded that the larger the values, the better the aerodynamic performance. However, an increase in each parameter value will increase the motor drive torque and the inertia moment of the flapping driving mechanism, especially when the flapping wing has a quick-return movement. This phenomenon increases the burden of the drive motor and its structure. Besides, the motion parameters are limited by the lever length parameters and transmission capacity. Therefore, further model optimization is needed to make the flapping wing generate more lift. Since there is a correlation between the flapping amplitude and the quick-return characteristics, both should be optimized to find the optimal structure.

Scientists have provided a numerical calculation method based on a given stroke speed ratio coefficient, a flapping angle value, a crank length value, and any other rod length values to determine the remaining rod length values. Notably, the crank of the flapping driving mechanism is redefined to be at a crank length of 3.48 mm. In the optimization model, to facilitate the solution, the rods shown in

Table 2 Wing stiffness of the experimental setup.

Wing vein diameter, mm	Wing mass, g
[0.5 (internal rod), 0.5 (external rod)]	1.3
[0.5, 0.8]	1.55
[0.5, 1.0]	1.75
[0.8, 0.8]	1.8

Fig. 2 are renamed $OA = a$, $AB = b$, $OB = c$, and $O_1O_2 = d$. Eqs. (18) - (21) give a method to determine the connecting rod length b, the frame length d, and the minimum transmission angle γ_{min} using the given crank length a, rocker length c, quick-return characteristic k, and flapping amplitude φ.

$$b = \sqrt{\frac{a^2\left(\cos\theta + 1\right) - 2c^2\sin\left(\frac{\varphi}{2}\right)^2}{\cos\theta - 1}} \tag{18}$$

$$d = \sqrt{c^2 + (b-a)^2 - 2(b-a)c\sin(\frac{\varphi}{2} - \theta - \arccos[\frac{c^2\sin^2\frac{\varphi}{2} + ab}{(a+b)c\sin\frac{\varphi}{2}}])} \tag{19}$$

$$\gamma_{min} = \arccos\frac{b^2 + c^2 - (d-a)^2}{2bc} \tag{20}$$

where $\theta = 180° \cdot \frac{k-1}{k+1}$ (21)

When φ is constant, k increases with decreasing γ_{min}, and the maximization function can be converted to a minimization function.

Therefore, given crank length and flapping amplitude, the connecting rod length b, frame length d, and γ_{min} can be determined by the rocker length and level of quick-return characteristic. The optimization model selects rocker length and stroke speed ratio coefficient as design variables, given by Eq. (22).

$$\vec{X} = [x_1, x_2]^T = [c, k]^T \tag{22}$$

The objective function can be expressed as Eq. (23) using the sum of squares of differences between $\cos\gamma_{min}$ and $\cos[\gamma]$.

$$F(\vec{X}) = [\cos[\gamma] - \frac{b^2 + c^2 - (d-a)^2}{2bc}]^2 \tag{23}$$

Considering that the overall FWMAV size should be small, the length of the rocker should not be limited to $[0.008\,m, 0.014\,m]$, and $k \in [1, 2]$. Hence, the restrictions are set by Eq. (24), where $\gamma_{min} \geq [\gamma] = 40$ deg.

$$\begin{aligned}
a + b &\leq c + d \\
a + c &\leq b + d \\
a + d &\leq b + c \\
a &\leq b, a \leq b, a \leq b \\
\cos\gamma_{min} &\leq \cos[\gamma]
\end{aligned} \tag{24}$$

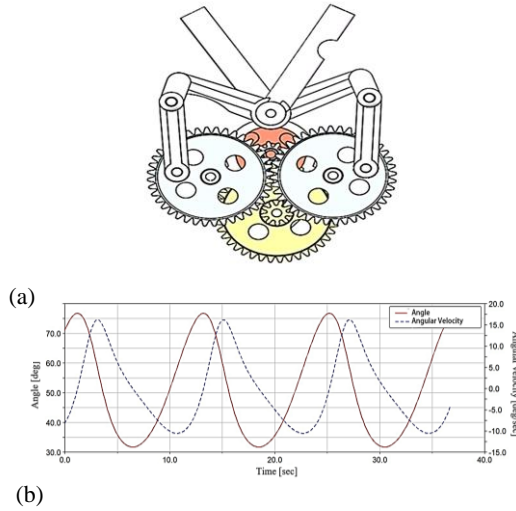To meet the allowable transmission angle value, the

(a)

(b)

Fig. 15. (a) Schematic of the optimized flapping driving mechanism, and (b) time histories of angular displacement and angular velocity of the optimized model.

optional design interval for the flapping amplitude is from 25 to 47 deg and the interval for the quick-return coefficient (level of quick-return characteristics) is [1.196, 1.324]. The experimental setting is arranged in Table 3. No. 13 has the highest average lift (0.260 N) with a quick-return coefficient and a flapping amplitude of 1.282 and 45°, respectively. A comparison between the average lift in the preliminary design and this optimized value demonstrates that the new design brings a 15% lift improvement to FWMAV. The parameters of the new design are listed in Table 4. Figure 15 (a) shows the new physical model after optimization. The variation curves of angular velocity displacement and angular velocity acceleration displacement are shown in Fig. 15 (b).

4. CONCLUSION

A prototype of a flapping wing micro air vehicle is designed to achieve multi-attitude flight. The whole process has three steps: preliminary design, simulated and experimental aerodynamic analyses, and aerodynamic optimization. A preliminary design was conducted to complete the basic flapping flight posture. The aerodynamic analysis generates the best parameter settings, based on particle hydrodynamic behavior. The relationship between key design parameters (e.g., flapping wing frequency, flapping

Table 3 Optimized iteration for the average lift.

No.	k_{max}	φ_{max}, °	$\overline{F_l}$, N
1	1.322	25	0.229
2	1.324	26	0.230
3	1.323	28	0.233
4	1.321	30	0.235
5	1.319	32	0.234
6	1.316	34	0.236
7	1.310	35	0.238
8	1.311	37	0.242
9	1.302	40	0.250
10	1.297	41	0.251
11	1.277	42	0.248
12	1.289	44	0.258
13	1.282	45	0.260
14	1.257	46	0.252

wing amplitude, and quick-return characteristics) and aerodynamic force is derived. The unique role of the quick-return characteristic on the aerodynamic characteristics and the couplings and constraints of the various design parameters are generated. The proposed experiments verify the accuracy of the simulated analysis. An aerodynamic influencing factor (wing flexibility) is simultaneously explored and the optimized flapping wing driving mechanism and wing design parameters derived. Considering the constraints of the FWMAV mechanism design, the optimized flapping wing frequency and amplitude are set at 20 Hz and 45 deg, respectively, and the optimized quick-return characteristic is at 1.282. The average lift is increased by 15 % to 0.260 N by optimizing the flapping wing drive mechanism. In addition, the exploration of the flexibility of the wings shows that the optimized wing layout is Wing8235, and optimal wing stiffness is achieved when the wing vein diameter is set to [0.5, 0.8] mm.

The limitation of this paper is that uncertainties of FWMAV are not concerned. Future studies will focus on quantifying and analyzing uncertainties in experimental and manufacturing processes. Reliability-based design and optimization will be carried out to improve flight stability.

Table 4 Final design parameters.

Crank a, mm	Connecting rod b, mm	Rocker c, mm	Frame d, mm	k	φ_{max}, deg	γ, deg
3.48	8.96	10.00	10.04	1.282	45	40.02

REFERENCES

Apker, T. B. and T. C. Corke (2015). Experiments and modeling of micro flapping wings of different designs in hover. *AIAA Journal* 53(3), 542-553.

Arastehfar, S., C. M. Chew, A. Jalalian, G. Gunawan and K. S. Yeo (2019). A relationship between sweep angle of flapping pectoral fins and thrust generation. *Journal of Mechanisms and Robotics* 11(1), 011014.

Armanini, S. F., J. V. Caetano, G. de Croon, C. C. de Visser and M. Mulder (2016). Quasi-steady aerodynamic model of clap-and-fling flapping MAV and validation using free-flight data. *Bioinspiration & Biomimetics* 11(4), 046002.

Bharadwaj, A. S. and S. Ghosh (2020). Numerical investigation of lift enhancement in flapping hover flight. *Physics of Fluids* 32(5), 051901.

Cho, H., J. Kwak, S. Shin, N. Lee and S. Lee (2016). Flapping-wing fluid–structural interaction analysis using corotational triangular planar structural element. *AIAA Journal* 54(8), 2265-2276.

Combes, S. A. and T. L. Daniel (2003). Into thin air: contributions of aerodynamic and inertial-elastic forces to wing bending in the hawkmoth Manduca sexta. *Journal of Experimental Biology* 206(17), 2999-3006.

Cros, A., B. Franco Llamas and E. Sandoval Hernández (2018). Vortical patterns generated by flapping foils of variable ratio chord-to-thickness. *Experiments in Fluids* 59(10), 1-9.

Deng, S., M. Perçin, B. W. van Oudheusden, H. Bijl, B. Remes and T. Xiao (2017). Numerical simulation of a flexible x-wing flapping-wing micro air vehicle. *AIAA Journal* 55(7), 2295-2306.

Dong, Y., B. Song, D. Xue and W. Yang (2022). 3D Numerical Simulation of a Hovering Hummingbird-inspired Flapping Wing with Dynamic Morphing. *Journal of Applied Fluid Mechanics* 15(3), 873-888.

Ellington, C. P. (1984). The aerodynamics of hovering insect flight. II. Morphological parameters. *Philosophical Transactions of the Royal Society of London. B, Biological Sciences* 305(1122), 17-40.

Floreano, D. and R. J. Wood (2015). Science, technology and the future of small autonomous drones. *Nature* 521(7553), 460-466.

Heathcote, S. and I. Gursul (2007). Flexible flapping airfoil propulsion at low Reynolds numbers. *AIAA Journal* 45(5), 1066-1079.

Kajak, K. M., M. Karásek, Q. P. Chu and G. C. H. E. De Croon (2019). A minimal longitudinal dynamic model of a tailless flapping wing robot for control design. *Bioinspiration & Biomimetics* 14(4), 046008.

Karásek, M., F. T. Muijres, C. De Wagter, B. D. Remes and G. C. De Croon (2018). A tailless aerial robotic flapper reveals that flies use torque coupling in rapid banked turns. *Science* 361(6407), 1089-1094.

Keennon, M., K. Klingebiel and H. Won (2012, January). Development of the nano hummingbird: A tailless flapping wing micro air vehicle. In *50th AIAA Aerospace Sciences Meeting Including the New Horizons Forum and Aerospace Exposition,* Nashville, USA.

Kumar, G. V. and D. A. Shah (2017). Aerodynamics of Flapping Wings for Vertical Takeoff. *Journal of Applied Fluid Mechanics* 10(6), 1689-1697.

Li, F., P. Yu, N. Deng, G. Li and X. Wu (2022). Numerical Analysis of the Effect of the Non-Sinusoidal Trajectories on the Propulsive Performance of a Bionic Hydrofoil. *Journal of Applied Fluid Mechanics* 15(3), 17-925.

Liu, Q., Q. Li, X. Zhou, P. Xu, L. Ren and S. Pan (2019). Development of a novel flapping wing micro aerial vehicle with elliptical wingtip trajectory. *Mechanical Sciences* 10(2), 355-362.

Martínez Gallar, B., B. W. van Oudheusden, A. Sciacchitano and M. Karásek (2020). Large-scale volumetric flow visualization of the unsteady wake of a flapping-wing micro air vehicle. *Experiments in Fluids* 61(1), 1-21.

Mayo, D. B., J. L. Lankford, M. Benedict and I. Chopra (2015). Experimental and computational analysis of rigid flapping wings for micro air vehicles. *Journal of Aircraft* 52(4), 1161-1178.

Nguyen, Q. V., W. L. Chan and M. Debiasi (2017). Experimental investigation of wing flexibility on force generation of a hovering flapping wing micro air vehicle with double wing clap-and-fling effects. *International Journal of Micro Air Vehicles* 9(3), 187-197.

Perçin, M., B. W. van Oudheusden, G. C. H. E. De Croon and B. Remes (2016). Force generation and wing deformation characteristics of a flapping-wing micro air vehicle 'DelFly II' in hovering flight. *Bioinspiration & biomimetics* 11(3), 036014.

Phan, H. V., Q. T. Truong and H. C. Park (2017). An experimental comparative study of the efficiency of twisted and flat flapping wings during hovering flight. *Bioinspiration & Biomimetics* 12(3), 036009.

Qadri, M., A. Shahzad, F. Zhao and H. Tang (2019). An experimental investigation of a passively flapping foil in energy harvesting mode. *Journal of Applied Fluid Mechanics* 12(5), 1547-1561.

Sane, S. P. (2003). The aerodynamics of insect flight. *Journal of Experimental Biology* 206(23), 4191-4208.

Seshadri, P., M. Benedict and I. Chopra (2013). Understanding micro air vehicle flapping-wing aerodynamics using force and flowfield measurements. *Journal of Aircraft* 50(4), 1070-1087.

Shahzad, A., M. Qadri and S. Ahmad (2019). Numerical analysis of high aspect ratio flexible wings in flapping motion. *Journal of Applied Fluid Mechanics* 12(6), 1979-1988.

Shyy, W., C. K. Kang, P. Chirarattananon, S. Ravi and H. Liu (2016). Aerodynamics, sensing and control of insect-scale flapping-wing flight. *Proceedings of the Royal Society A: Mathematical, Physical and Engineering Sciences* 472(2186), 20150712.

Shyy, W., H. Aono, C. K. Kang and H. Liu (2013). *An Introduction to Flapping Wing Aerodynamics*. Cambridge University Press. Cambridge, UK.

Shyy, W., M. Berg and D. Ljungqvist (1999). Flapping and flexible wings for biological and micro air vehicles. *Progress in aerospace sciences* 35(5), 455-505.

Syam Narayanan, S. and R. Asad Ahmed (2021). Effect of Fluid-Structure Interaction on Noise Generation in MAV with Fixed and Flapping Membrane Wing. *Journal of Applied Fluid Mechanics* 14(6), 1817-1826.

Tay, W. B., B. W. van Oudheusden and H. Bijl (2015). Numerical simulation of a flapping four-wing micro-aerial vehicle. *Journal of Fluids and Structures* 55, 237-261.

Wang, Z. J., J. M. Birch and M. H. Dickinson (2004). Unsteady forces and flows in low Reynolds number hovering flight: two-dimensional computations vs robotic wing experiments. *Journal of Experimental Biology* 207(3), 449-460.

Zhang, J., B. Cheng, B. Yao and X. Deng, (2015, May). Adaptive robust wing trajectory control and force generation of flapping wing MAV. In *2015 IEEE International Conference on Robotics and Automation (ICRA)*, Seattle, USA.